Nonlinear M-shaped broadband piezoelectric energy harvester for very low base accelerations: primary and secondary resonances

S Leadenham and A Erturk

G W Woodruff School of Mechanical Engineering, Georgia Institute of Technology, Atlanta, GA 30332, USA

E-mail: alper.erturk@me.gatech.edu

CrossMark

Abstract

It has been well demonstrated over the past few years that vibration energy harvesters with intentionally designed nonlinear stiffness components can be used for frequency bandwidth enhancement under harmonic excitation for sufficiently high vibration amplitudes. In order to overcome the need for high excitation intensities that are required to exploit nonlinear dynamic phenomena, we have developed an M-shaped piezoelectric energy harvester configuration that can exhibit a nonlinear frequency response under very low vibration levels. This configuration is made from a continuous bent spring steel with piezoelectric laminates and a proof mass but no magnetic components. Careful design of this nonlinear architecture that minimizes piezoelectric softening further enables the possibility of achieving the jump phenomenon in hardening at few milli-g base acceleration levels. In the present work, such a design is explored for both primary and secondary resonance excitations at different vibration levels and load resistance values. Following the primary resonance excitation case that offers a 660% increase in the half-power bandwidth as compared to the linear system at a root-mean-square excitation level as low as $0.04g$, secondary resonance behavior is investigated with a focus on 1:2 and 1:3 superharmonic resonance neighborhoods. A multi-term harmonic balance formulation is employed for a computationally effective yet high-fidelity analysis of this high-quality-factor system with quadratic and cubic nonlinearities. In addition to primary resonance and secondary (superharmonic) resonance cases, multi-harmonic excitation is modeled and experimentally validated.

Keywords: energy harvesting, piezoelectricity, nonlinear vibration, nonlinear dynamics

(Some figures may appear in colour only in the online journal)

1. Introduction

The transformation of ambient vibration into low-power electricity for powering small electronic components (e.g. wireless sensors) has received growing attention over the last decade [1–3] to enable energy-autonomous systems. Various research groups have reported their work on modeling and applications of vibration-based energy harvesting using electromagnetic [4–6], electrostatic [7–9], piezoelectric [10–13] and magnetostrictive [14, 15] transduction mechanisms, as well as the use of electronic and ionic electroactive polymers [16, 17] and polymer electrets [18], and even flexoelectricity for energy harvesting at submicron scales [19]. Among the basic transduction mechanisms that can be used for vibration-to-electricity conversion, piezoelectric transduction has received the most attention due to the high power density and ease of application of piezoelectric materials [2, 20, 21].

Theoretical and experimental aspects of linear-resonant piezoelectric energy harvesting have been researched extensively in the first decade of this century [10–13]. A major limitation in the commonly employed resonant energy harvester configuration is that the effective power generation performance of the device is limited to resonance excitation. Especially in high-quality-factor piezoelectric energy harvesters, if the excitation frequency deviates slightly from the fundamental linear resonance frequency of the harvester (as a result of manufacturing imperfections or changing excitation and/or environmental conditions), the electrical power output is drastically reduced by orders of magnitude. To overcome this bandwidth issue of conventional linear-resonant configurations, researchers have recently investigated exploitation of nonlinear dynamic phenomena [22–24]. For the broad literature of nonlinear energy harvesting, the reader is referred to a recent comprehensive review article [25]. Only a brief review is given in the next paragraph.

Early investigations of exploiting nonlinear stiffness in electromagnetic energy harvesting were due to Burrow *et al* [26] and Mann and Sims [27] using monostable Duffing oscillators. Arguably the first intentionally-designed nonlinear piezoelectric energy harvester architectures were published independently by Cottone *et al* [28] and Erturk *et al* [29] in early 2009. Using two different bistable 'piezo-magnetoelastic' structures, the former group explored noise (random) excitation [28] while the latter one [29] explored harmonic excitation with a focus on broadband interwell periodic oscillations. Another seminal paper was due to Stanton *et al* [30] who showed bidirectional increase of the frequency bandwidth in a monostable 'magnetopiezoelastic' configuration. After this explosion of pioneering research in nonlinear energy harvesting, numerous other papers appeared on exploiting nonlinear dynamic phenomena in vibration energy harvesting. Other than magnetoelastic interactions [29–34], purely elastic buckling was also considered for bandwidth and performance enhancement in nonlinear energy harvesting [35, 36]. A bistable electromagnetic energy harvester was theoretically and experimentally explored by Mann and Owens [37]. In electrostatic energy harvesting, MEMS bistable spring arrangements for bandwidth enhancement were presented by Nguyen *et al* [38]. Stanton *et al* [32] theoretically investigated bifurcations of a bistable configuration similar to the one tested by Cottone *et al* [39], and presented harmonic balance analysis using a single harmonic [34]. Ramlan *et al* [40] explored hardening stiffness in monostable Duffing oscillator along with snap-through behavior in a mass-spring-damper mechanism. Two research groups reported superharmonic resonance behaviors in monostable [41] and bistable [42] energy harvesters. Other than the aforementioned intentionally designed nonlinearities, inherent electroelastic and dissipative nonlinearities in piezoelectric energy harvesting were studied by Stanton *et al* [43–45] and most recently by Leadenham and Erturk [46] to establish a unified framework. Others investigated random excitation of nonlinear energy harvesters [47–52], which is beyond the scope of our current paper.

Under harmonic excitation, typically the greatest bandwidth enhancement can be achieved in the presence of strong nonlinearities and under hard (strong) excitation [22]. For instance, to overcome the potential barrier in bistable energy harvesters and exploit broadband interwell periodic oscillations [29], the required excitation levels are typically [29–36] on the order of 0.5–1g (where $g = 9.81$ m s^{-2}). This presents a challenge for nonlinear energy harvesting in low-intensity vibration environments. Furthermore, most meso-scale nonlinear energy harvesters use discrete components (e.g. magnets) and magnetoelastic interactions to create the desired nonlinear stiffness. Such designs are relatively complex and magnetic interactions may not be allowable in some environments. To avoid these potential issues, we have developed an M-shaped bent spring steel asymmetric oscillator for nonlinear bandwidth enhancement as a simple but effective design for piezoelectric and/or electromagnetic energy harvesting (inspired by its MEMS counterpart [53] used for electrostatic energy harvesting).

In our recent effort [54] focusing on purely mechanical (structural) dynamics of this configuration, it was suggested that broadband energy harvesting can be achieved for excitations below 0.1g base acceleration. In the following, we introduce an M-shaped piezoelectric energy harvester prototype, present its empirical mathematical model, and investigate its linear and nonlinear electromechanical dynamics by rigorous experiments and high-fidelity modeling using the method of harmonic balance with multiple terms. Both primary resonance and secondary resonance (for superharmonic response) behaviors, as well as multi-harmonic excitation, are modeled and experimentally validated.

2. Nonlinear piezoelectric energy harvester, mathematical description, and analysis

2.1. M-shaped piezoelectric energy harvester

3D model and photographic views of the nonlinear M-shaped piezoelectric energy harvester prototype explored in this work are shown in figure 1 along with its clamp and shaker mount. While this device can be fabricated at different geometric scales, the M-shaped energy harvester analyzed in this work consists of a flexible beam made from 25.4 mm wide by 0.254 mm thick AISI 1075 spring steel and is approximately 22 cm long. The steel is cut and bent using common sheet metal tools. The bend angles used are small enough to allow near zero radius bends without first heating the metal. The lumped mass attachment consists of pieces of stainless steel, bolted together sandwiching the center of the beam. Both ends of the bent beam are clamped. The clamp and shaker mount are made from 6061 aluminum. Electromechanical coupling is due to four piezoelectric patches bonded near the clamps (resulting in two bimorphs bracketing the continuous spring steel substrate). Dynamic bending of the spring causes tensile and compressive strains on the piezoelectric layers, yielding an alternating voltage via the direct piezoelectric effect, which is then connected to an electrical load for AC
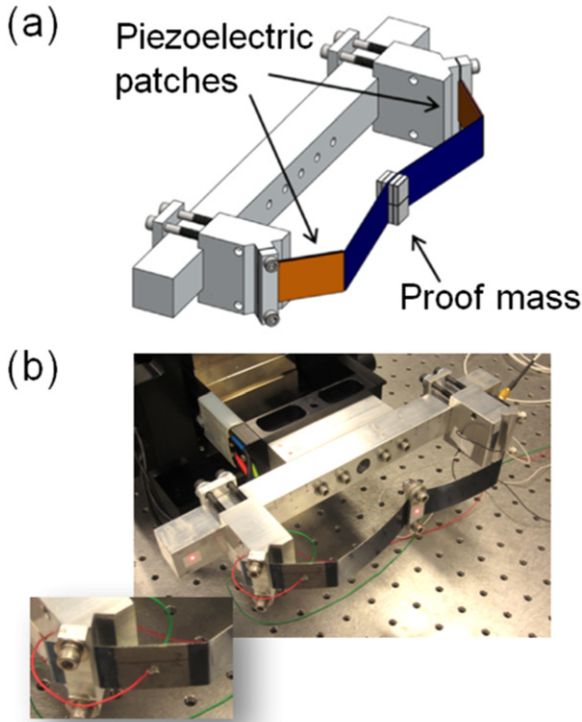
Figure 1. (a) 3D model and (b) picture of the nonlinear M-shaped piezoelectric energy harvester prototype along with its clamp and shaker mount. Close-up picture shows one of the four piezoelectric patches (which form two bimorphs).

power generation (or it can be rectified and conditioned in an energy harvesting circuit to obtain a stable DC signal for charging a storage component). The present effort focuses on analyzing the AC power generation characteristics and harmonic balance analysis of this nonlinear piezoelectric energy harvester when excited near its primary or secondary (superharmonic) resonance frequencies.

2.2. Governing electromechanical equations

The M-shaped energy harvester is modeled as a single-degree-of-freedom system undergoing base excitation with linear viscous and quadratic damping terms, a nonlinear elastic restoring force, and linear electromechanical coupling (figure 2). The locations of the piezoelectric patches in figure 1(b) are chosen to reduce piezoelectric softening non-linearity [46] and best exploit the geometric hardening non-linearity of the M-shaped design[1]. The force balance and current balance equations are then

$$m\ddot{z} + b\dot{z} + b_a \, |\dot{x}| \, \dot{x} + F_s(z) - \theta v = -\bar{m}\ddot{y}, \tag{1}$$

[1] Piezoelectric material nonlinearity in energy harvesting is manifested in the form of ferroelastic softening (of quadratic order—from the dynamical system standpoint—according to our recent work [46]), which would inherently eliminate a significant part of the geometric hardening bandwidth (before it appears) in the case of tightly clamped piezoelectrics at the roots. Therefore piezoelectric patches are deliberately located slightly outside the clamps to reduce the strain in piezoelectrics. This is a tradeoff between the peak power output and the frequency bandwidth, and clearly the effort presented here is concerned with the latter.
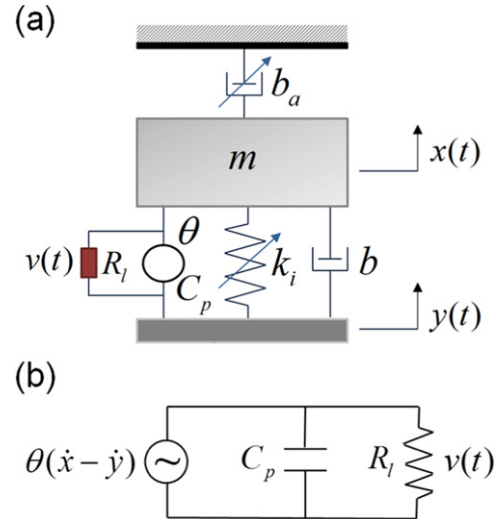

Figure 2. (a) Lumped-parameter electromechanical model and (b) equivalent circuit model with a dependent current source and linear electromechanical coupling.

$$C_p \dot{v} + \frac{1}{R_l} v + \theta \dot{z} = 0, \tag{2}$$

where m is the equivalent mass of the device, $\bar{m}$ is the effective mass that causes the forcing term due to base excitation ($m \cong \bar{m}$ if the lumped mass dominates the mass of the rest of the structure), b is the linear viscous damping coefficient, b_a is the quadratic (velocity-squared) damping coefficient (typically attributed to fluid-structure interaction), $F_s(z)$ is the nonlinear elastic restoring force, $y(t)$ is the base displacement measured in an inertial frame, $z(t)$ is the displacement of the oscillator relative to the moving base, $x(t)$ is the displacement of the mass relative to the fixed reference frame (i.e. $x(t) = y(t) + z(t)$), and an overdot represents differentiation with respect to time.

2.3. Harmonic balance analysis: general multi-harmonic formulation

The second-order force balance equation with nonlinear terms and linear current balance equation given by equations (1) and (2) can be expressed in the form of three first-order equations for time-domain numerical simulations (e.g. by using ode45 in MATLAB). However, the process of numerical simulation in time domain can be computationally lengthy (especially to reach steady state in high-quality-factor systems), and it offers little or no insight into the underlying mathematics of the problem. Among the methods of approximate analytical solutions for nonlinear differential equations, the method of harmonic balance [22, 54, 55] is preferred in this work, since the system studied here exhibits a high degree of nonlinearity (strong nonlinearity) and therefore it is required to explore multi-harmonic solutions for enhanced accuracy [54]. In the following, first the multi-harmonic solution is given by accounting for higher harmonics and a DC (constant) component prior to demonstrating the solution process for the case of a single harmonic.

The base excitation term is assumed to be harmonic of the form:

$$\ddot{y}(t) = A\cos(\Omega t), \tag{3}$$

where A is the base acceleration amplitude and Ω is the driving frequency. It is useful to write the governing in state-space form:

$$x_1 = z, \quad x_2 = \dot{z}, \quad x_3 = v. \tag{4}$$

The governing equations then become the first order system of ordinary differential equations:

$$\dot{x}_1 = x_2,$$

$$\dot{x}_2 = \frac{1}{m}\left[-bx_2 - b_a \left| x_2 + \frac{A}{\Omega}\sin(\Omega t) \right| \right.$$
$$\left. \times \left(x_2 + \frac{A}{\Omega}\sin(\Omega t) \right) - F_s(x_1) + \theta x_3 - \bar{m}A\cos(\Omega t) \right],$$

$$\dot{x}_3 = \frac{-1}{C_p}\left(\frac{1}{R_l}x_3 + \theta x_2 \right) \tag{5}$$

which can be written in vector form:

$$\dot{\vec{x}} = \vec{f}(t, \vec{x}) = \vec{f}(t + T, \vec{x}). \tag{6}$$

This system with explicit time dependence is periodic in time with period $T = 2\pi/\Omega$. A truncated Fourier series solution with N harmonics and the same period is assumed for solution:

$$\vec{x}(t) = \vec{a} + \mathbf{A}\vec{c}(t) + \mathbf{B}\vec{s}(t), \tag{7}$$

where $\vec{a}$ is a constant vector representing the DC components of the response, $\mathbf{A}$ and $\mathbf{B}$ are constant 3xN rectangular matrices containing the cosine and sine coefficients, while $\vec{c}(t)$ and $\vec{s}(t)$ are vectors of cosine and sine functions defined as

$$c_n(t) = \cos(n\Omega t),$$
$$s_n(t) = \sin(n\Omega t). \tag{8}$$

With the chosen approximate solution, the residual function is

$$\vec{r}(t) = \vec{f}(t, \vec{x}(t)) - \dot{\vec{x}}(t). \tag{9}$$

In order to find the unknowns $\vec{a}$, $\mathbf{A}$, and $\mathbf{B}$, the residual function is minimized in the Galerkin method sense such that

$$\int_0^{2\pi/\Omega} \vec{r}(t)\mathrm{d}t = 0,$$

$$\int_0^{2\pi/\Omega} \vec{r}(t)\vec{c}^{\mathrm{T}}(t)\mathrm{d}t = 0,$$

$$\int_0^{2\pi/\Omega} \vec{r}(t)\vec{s}^{\mathrm{T}}(t)\mathrm{d}t = 0. \tag{10}$$

This yields $3(2N+1)$ equations for the same number of unknowns. This nonlinear system of algebraic equations can be solved in a number of ways, one of the best being the Newton–Raphson method.

2.4. Single-harmonic formulation and frequency response equations

While the main advantage of harmonic balance analysis is the ease of including higher harmonics in a systematic way, consider the simplest solution using only the constant term and first frequency component, i.e. $N = 1$, in order to illustrate the solution process. The assumed solutions for the relative displacement, relative velocity, and electrode voltage are

$$z(t) = x_1(t) = a_1 + A_{11}\cos(\Omega t) + B_{11}\sin(\Omega t), \tag{11}$$

$$\dot{z}(t) = x_2(t) = a_2 + A_{21}\cos(\Omega t) + B_{21}\sin(\Omega t), \tag{12}$$

$$v(t) = x_3(t) = a_3 + A_{31}\cos(\Omega t) + B_{31}\sin(\Omega t) \tag{13}$$

which yield the following residual functions:

$$r_1(t) = a_2 + A_{21}\cos(\Omega t) + B_{21}\sin(\Omega t)$$
$$+ A_{11}\Omega\sin(\Omega t) - B_{11}\Omega\cos(\Omega t), \tag{14}$$

$$r_2(t) = m\Omega\left[-A_{21}\sin(\Omega t) + B_{21}\cos(\Omega t) \right]$$
$$+ b\left[a_2 + A_{21}\cos(\Omega t) + B_{21}\sin(\Omega t) \right]$$
$$+ b_a \left| a_2 + A_{21}\cos(\Omega t) + \left(B_{21} + \frac{A}{\Omega} \right)\sin(\Omega t) \right|$$
$$\times \left[a_2 + A_{21}\cos(\Omega t) + \left(B_{21} + \frac{A}{\Omega} \right)\sin(\Omega t) \right]$$
$$+ k_1\left(a_1 + A_{11}\cos(\Omega t) + B_{11}\sin(\Omega t) \right)$$
$$+ k_2\left[a_1 + A_{11}\cos(\Omega t) + B_{11}\sin(\Omega t) \right]^2$$
$$+ k_3\left[a_1 + A_{11}\cos(\Omega t) + B_{11}\sin(\Omega t) \right]^3$$
$$+ k_4\left[a_1 + A_{11}\cos(\Omega t) + B_{11}\sin(\Omega t) \right]^4$$
$$+ k_5\left[a_1 + A_{11}\cos(\Omega t) + B_{11}\sin(\Omega t) \right]^5$$
$$- \theta\left[a_3 + A_{31}\cos(\Omega t) + B_{31}\sin(\Omega t) \right]$$
$$+ \bar{m}A\cos(\Omega t), \tag{15}$$

$$r_3(t) = C_p\Omega\left[-A_{31}\sin(\Omega t) + B_{31}\cos(\Omega t) \right]$$
$$+ \frac{1}{R_l}\left[a_3 + A_{31}\cos(\Omega t) + B_{31}\sin(\Omega t) \right]$$
$$+ \theta\left[a_2 + A_{21}\cos(\Omega t) + B_{21}\sin(\Omega t) \right]. \tag{16}$$

Minimizing the residual functions in the Galerkin sense (equation (10)) means finding the unknowns (elements of $\vec{a}$, $\mathbf{A}$, and $\mathbf{B}$) such that each of the residual functions is orthogonal to each of the basis functions: 1, $\cos(\Omega t)$, and $\sin(\Omega t)$ in this particular case of $N = 1$. Carrying out the required integrations yields the following system of nine nonlinear algebraic equations for the nine unknown Fourier coefficients in equations (11)–(13):

$$a_2 = 0, \tag{17}$$

$$A_{21} - \Omega B_{11} = 0, \tag{18}$$

$$B_{21} + \Omega A_{11} = 0, \tag{19}$$

$$3k_3 a_1 A_{11}^2 + 3k_3 a_1 B_{11}^2 + 6k_4 a_1^2 A_{11}^2 + 6k_4 a_1^2 B_{11}^2$$

$$+ \frac{3}{2} k_4 A_{11}^2 B_{11}^2 + 10 k_5 a_1^3 A_{11}^2 + 10 k_5 a_1^3 B_{11}^2$$

$$+ \frac{15}{4} k_5 a_1 A_{11}^4 + \frac{15}{4} k_5 a_1 B_{11}^4 + k_2 A_{11}^2 + k_2 B_{11}^2$$

$$+ 2k_3 a_1^3 + \frac{3}{4} k_4 A_{11}^4 + \frac{3}{4} k_4 B_{11}^4$$

$$+ 2k_4 a_1^4 + 2k_5 a_1^5 - 2\theta a_3 + 2b_{eq} a_2$$

$$+ 2k_1 a_1 + 2k_2 a_1^2 + \frac{15}{2} k_5 a_1 A_{11}^2 B_{11}^2 = 0, \qquad (20)$$

$$\frac{3}{4} k_3 A_{11}^3 + \bar{m} A + \frac{5}{8} k_5 A_{11}^5 + b_{eq} A_{21} + k_1 A_{11}$$

$$- \theta A_{31} + 3k_4 a_1 A_{11} B_{11}^2 + \frac{15}{2} k_5 a_1^2 A_{11} B_{11}^2$$

$$+ \frac{5}{8} k_5 A_{11} B_{11}^4 + \frac{15}{2} k_5 a_1^2 A_{11}^3 + 4k_4 a_1^3 A_{11}$$

$$+ 3k_4 a_1 A_{11}^3 + 5k_5 a_1^4 A_{11}$$

$$+ m\Omega B_{21} + 2k_2 a_1 A_{11} + 3k_4 a_1^2 A_{11}$$

$$+ \frac{5}{4} k_5 A_{11}^3 B_{11}^2 + \frac{3}{4} k_3 A_{11} B_{11}^2 = 0, \qquad (21)$$

$$- m\Omega A_{21} + 4k_4 a_1^3 B_{11} + 5k_5 a_1^4 B_{11} + 2k_2 a_1 B_{11}$$

$$+ 3k_3 a_1^2 B_{11} + \frac{5}{8} k_5 A_{11}^4 B_{11}$$

$$+ \frac{3}{4} k_3 A_{11}^2 B_{11} + \frac{5}{4} k_5 A_{11}^2 B_{11}^3 + 3k_4 a_1 B_{11}^3$$

$$+ \frac{15}{2} k_5 a_1^2 B_{11}^3 + b_{eq} B_{21} + k_1 B_{11}$$

$$+ \frac{5}{8} k_5 B_{11}^5 + \frac{3}{4} k_3 B_{11}^3 - \theta B_{31} + 3k_4 a_1 A_{11}^2 B_{11}$$

$$+ \frac{15}{2} k_5 a_1^2 A_{11}^2 B_{11} = 0, \qquad (22)$$

$$\theta a_2 + \frac{1}{R_l} a_3 = 0, \qquad (23)$$

$$C_p \Omega B_{31} + \frac{1}{R_l} A_{31} + \theta A_{21} = 0, \qquad (24)$$

$$C_p \Omega A_{31} - \frac{1}{R_l} B_{31} - \theta B_{21} = 0, \qquad (25)$$

where the first three equations confirm the expected relationship between z and $\dot{z}$. In these equations the dissipative terms have been combined by defining an equivalent viscous damping coefficient, b_{eq}, as

$$b_{eq} = b + \frac{8}{3\pi} b_a \sqrt{A_{21}^2 + B_{21}^2}. \qquad (26)$$

This is a very good approximation when the base velocity ($\dot{y}$) is small compared to the relative velocity ($\dot{z}$). This approximation is necessary, as integrating the quadratic dissipation term in closed form is impossible for general harmonic balance solutions with N harmonics. As is apparent, this system of equations is not solvable directly, and a numerical method such as Newton–Raphson is required to solve them. The difficulty of generating the system of

algebraic equations in closed form and the necessity of solving them numerically make it evident that, in practice, it is better to numerically generate and solve the system of nonlinear equations for harmonic balance analyses from the outset.

It is worth mentioning the approach used in the computational algorithm to obtain the harmonic balance analysis results presented in this work. A general harmonic balance solver is written to solve any system that can be written in the form of equation (6), which might include other nonlinearities (e.g. inertial [56], piezoelectric [46], and even circuit [57] nonlinearities). Since the integrations in equation (10) (and associated integrations to find elements of the Jacobian necessary for the Newton–Raphson method) are equivalent to finding Fourier series components, the algorithm's speed is significantly increased using fast Fourier transform (FFT) algorithms. In this way, harmonic balance analyses to find periodic solutions to high order/dimension systems can be completed orders of magnitude faster than time domain simulations, even while keeping many more harmonic components than is feasible with perturbation methods such as the Lindstedt–Poincaré method or the method of multiple scales [58]. The benefits over time domain simulation are especially apparent for high-quality-factor systems, where much computation time can be wasted simulating transients. Also by including the appropriate harmonics and choosing the correct driving frequency range, it is simple to use the method of harmonic balance to analyze secondary and combination resonances in addition to the primary resonance of a nonlinear oscillatory system.

2.5. Multi-harmonic excitation

Another advantage of the method of harmonic balance is the ease with which the analysis may be extended to include excitation from an arbitrary periodic source rather than a pure sinusoid. From the experimental standpoint, providing an ideal single frequency base acceleration is impossible, and in some circumstances, the contribution of harmonic distortion in the excitation to the response may not be negligible, which might yield misleading experimental results. For example, an ideal experiment to observe a quadratic superharmonic resonance would involve a single frequency excitation at $\Omega \approx \omega_n/2$, where ω_n is the linear natural frequency of the system. If a quadratic nonlinearity is present, a response at ω_n would be generated and then dynamically amplified, dominating the subresonant quasi-linear response at Ω. However, suppose the excitation (base acceleration) is *not* a pure sinusoid and instead is a general periodic function with form:

$$\ddot{y}(t) = p_0 + \sum_{n=1}^{\infty} p_n \cos(n\Omega t + \phi_n). \qquad (27)$$

In this case, the response at ω_n is due to both the quadratic nonlinearity as well as forcing at the natural frequency directly from the term with coefficient p_2. Experimentally, it is impossible to separate the superharmonic resonant response to the fundamental frequency of excitation signal from the quasi-linear resonant response due to higher harmonics of the
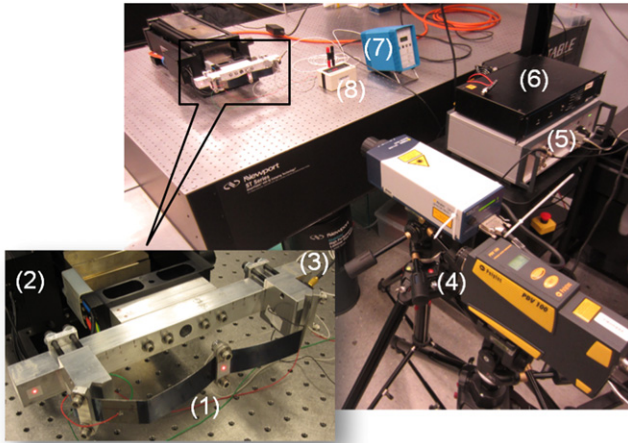
Figure 4. Experimental nonlinear static force versus displacement data (under short-circuit condition for the piezoelectric patches) and a quintic polynomial curve fit.

Figure 3. Experimental setup: (1) M-shaped nonlinear piezoelectric energy harvester; (2) vibration exciter (electrodynamic shaker); (3) accelerometer; (4) laser Doppler vibrometers; (5) vibration control unit (using base acceleration as the feedback signal); (6) power amplifier; (7) signal conditioner; and (8) resistance substitution (decade) box.

excitation signal. Therefore it is useful to be able to simulate response to multi-harmonic excitation to validate experiments and analyze differences between ideal experimental conditions and more realistic ones. Additionally, there might be practical scenarios of energy harvesting in which the ambient excitation form is indeed general periodic rather than simple harmonic.

3. Experimental results and model validation

3.1. Experimental procedure

In order to analyze the primary and secondary (super-harmonic) resonance energy harvesting performance of the device, as well as identify model parameters to simulate the system as previously discussed, a series of experiments are conducted. A static force–displacement test is completed to identify the nonlinear restoring force, F_s. Low amplitude linear regime energy harvesting tests are conducted to extract the equivalent mass, linear damping, and electromechanical coupling parameters. Finally nonlinear frequency sweep energy harvesting tests are reported for both primary and secondary (superharmonic) resonance excitation to evaluate the performance of the M-shaped energy harvester and the fidelity of the nonlinear electromechanical model and its harmonic balance analysis. Multi-harmonic excitation (as a part of secondary resonance excitation for superharmonic response) is also demonstrated and validated as an application of the model presented here.

3.2. Experimental setup for nonlinear dynamic analysis

An overview picture of the experimental setup is shown in figure 3 along with a close up view of the M-shaped piezoelectric energy harvester. Experiments are performed using an
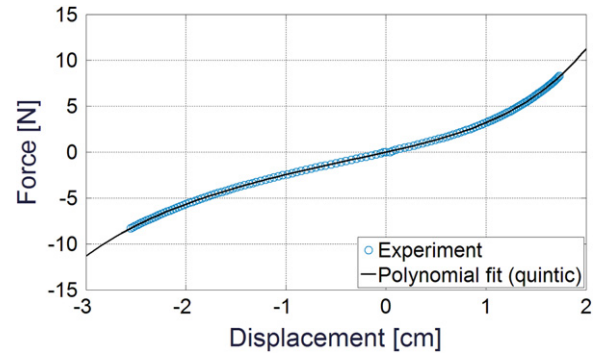
APS-113 seismic shaker driven by an APS-125 amplifier and controlled by a SPEKTRA VCS-201 controller. These devices allow for the sample to be subjected to harmonic base acceleration at specified amplitudes and frequencies. Tests consist of up and down frequency sweeps at a constant kinematic variable (in this case base acceleration amplitude) necessary for frequency response analysis of the nonlinear system. Base acceleration measured by a Kistler model 8636C50 ICP accelerometer is used for feedback to the VCS-201 controller. A Polytec PDV-100 Portable Digital Vibrometer is used to measure the base velocity. The velocity of the lumped mass (i.e. center of the M-shaped oscillator) is measured using a Polytec OFV-505 sensor head and OFV-5000 controller. Current output from the piezoelectric elements is shunted through a variable resistance box (IET Labs, RS-201W), the voltage across which is measured. A National Instruments NI USB-4431 unit is employed for data acquisition.

3.3. Parameter identification

In order to investigate the nonlinear system dynamics theoretically, it is necessary to identify the relevant parameters of the M-shaped energy harvester. First the relationship between deflection and restoring force (F_s) is extracted to empirically model the nonlinear stiffness behavior under short-circuit condition. To this end, the oscillator is bolted to the rigid optical table vertically (to set $y = 0$ so that $x = z$). The lumped mass attachment is removed (to avoid any sag due to gravity), and then weights are suspended from the center of the spring. Central deflection (z) is measured using the OFV-5000 displacement decoder of the laser vibrometer. The sample is turned over and the process repeated. It is assumed that the weight of the spring itself is negligible compared to the suspended weights. It is also assumed the removal of the mass attachments does not change the stiffness characteristics of the spring. The resulting force versus displacement curve is plotted in figure 4 along with a polynomial curve fit.

The following quintic (fifth-order) polynomial form is fit to the experimental nonlinear static force versus displacement

Table 1. Identified nonlinear spring coefficients.

k_1 (N cm^{-1})	k_2 (N cm^{-2})	k_3 (N cm^{-3})	k_4 (N cm^{-4})	k_5 (N cm^{-5})
2.441	0.286	0.363	0.103	0.021

Table 2. Identified mass, dissipation, electromechanical coupling, and capacitance terms.

m (g)	b (Ns m^{-1})	b_u (Ns^2 m^{-2})	θ (N V^{-1})	C_p (nF)
31.9	5.5×10^{-3}	1.2×10^{-2}	1.7×10^{-4}	34.27

data:

$$F_s(z) = k_1 z + k_2 z^2 + k_3 z^3 + k_4 z^4 + k_5 z^5. \qquad (28)$$

Here, the linear coefficient (k_1) can be interpreted as the linear spring stiffness for small displacements, while the higher order coefficients define the nonlinearity. Identified values of the stiffness coefficients are listed in table 1. The values of the coefficients are displayed with respect to a cm length scale, as this is the order of magnitude of displacements during nonlinear testing (note that the model obviously uses consistent SI units that take the displacement in meters in calculations). It is apparent that the quadratic and cubic terms dominate the nonlinearity, and are relatively comparable to each other in strength. Specifically, if the displacement is O (1) ('order 1' in cm scale) the cubic nonlinearity dominates the nonlinear part and comparable contribution is also due to the quadratic nonlinearity (this O(1) response physically happens for primary resonance excitation). On the other hand, if the displacement response is O(0.1) ('order 0.1' in cm-scale, or 'order 1' in mm-scale – which is expected to happen in secondary resonance excitation, e.g. superharmonic resonance), there is a predominant effect of quadratic nonlinearity, rather than cubic nonlinearity. This discussion will be revisited in the 'secondary resonance for super-harmonic response' section.

The equivalent mass, linear damping coefficient, and electromechanical coupling coefficients are obtained from linear energy harvesting resistor sweep experiments, and the harvester capacitance is measured directly. Note that the equivalent mass is simply $m = k_1/\omega_n^2$ (where ω_n is the short-circuit natural frequency). Linear viscous damping coefficient is simply $b = 2\zeta m \omega_n$, where the mechanical damping ratio (ζ) is identified from half-power points of the short-circuit vibration frequency response (it could as well be identified from free vibrations [54] under short-circuit condition by using the logarithmic decrement). Finally, the quadratic damping term, b_u, in equation (1) is found to account for overestimates of peak response with linear damping alone. The physical justification of quadratic (or velocity-squared) damping is nonlinear fluid damping [59, 60] associated with drag force resulting from large amplitude vibration. These model parameters are summarized in table 2.

3.4. Linear frequency response

The linear regime energy harvesting tests allow the measuring of the velocity, voltage, current, and power frequency response functions (FRFs) by means of white noise type random base excitation. For this system, white noise excitation is preferable to a chirp or sine sweep, because the threshold for nonlinear behavior is extremely low (which is

the advantage of the configuration to exploit nonlinear broadband behavior for low excitation intensities), on the order of $5 \times 10^{-3} g$ RMS base acceleration. A finite set of resistive loads has to be used in the experiments and it is preferable to cover a broad range between the short-circuit ($R_l \to 0$) and open-circuit ($R_l \to \infty$) extremes. While the system is not too weakly coupled, $R_l \cong 1/\omega_n C_p$ can be used to estimate the optimal load resistance neighborhood as an approximation. For this system, $1/\omega_n C_p$ yields approximately $300 \, \mathrm{k}\Omega$, so the range of $30 \, \mathrm{k}\Omega$ to $3 \, \mathrm{M}\Omega$ is selected to include electrical boundary conditions ranging from nearly short circuit to nearly open circuit.

Figure 5 shows the velocity, voltage, current and power FRFs for the five chosen load resistances. Once again, to eliminate strong piezoelectric softening nonlinearity [46], the level piezoelectric coupling is designed to be relatively low (as mentioned in section 2.2) by locating the piezoceramic patches outside the clamps, and therefore the short- and open-circuit resonance frequencies are quite close, approximately 13.91 and 13.94 Hz, respectively. In the linear regime, mechanical dissipation is extremely light, with a viscous damping ratio of $\zeta \cong 0.001$ (identified from the short-circuit voltage FRF). As anticipated, the 300kΩ load is a reasonable approximation to the optimal electrical load neighborhood, yielding a peak normalized power of approximately 5.4 W/g^2 (linear estimate). As the linear model parameters are extracted empirically, the model yields an excellent match in figure 5. It should be noted that the linear system has very low bandwidth (0.05 Hz for $300 \, \mathrm{k}\Omega$ load resistance). It is of interest how much this bandwidth increases with increased base acceleration levels, which is discussed next.

3.5. Nonlinear frequency response

The nonlinear energy harvesting experiments consist of controlled (i.e. constant base acceleration) up and down frequency sweeps to capture the jump phenomenon associated with saddle-node bifurcation [23, 24] that provides nonlinear bandwidth enhancement. Primary resonance tests refer to excitation frequencies that are near the linear natural frequency of the energy harvester, i.e. $\Omega \approx \omega_n$. In this work, secondary resonance behavior refers to excitation that is either one half or one third of the linear natural frequency (i.e. rather than subharmonic we focus on these superharmonic resonances). In the case of the one half secondary resonance, excitation at Ω will yield a response at $2\Omega \approx \omega_n$ that will resonate. Similarly, the one third secondary resonance would involve a response at $3\Omega \approx \omega_n$.
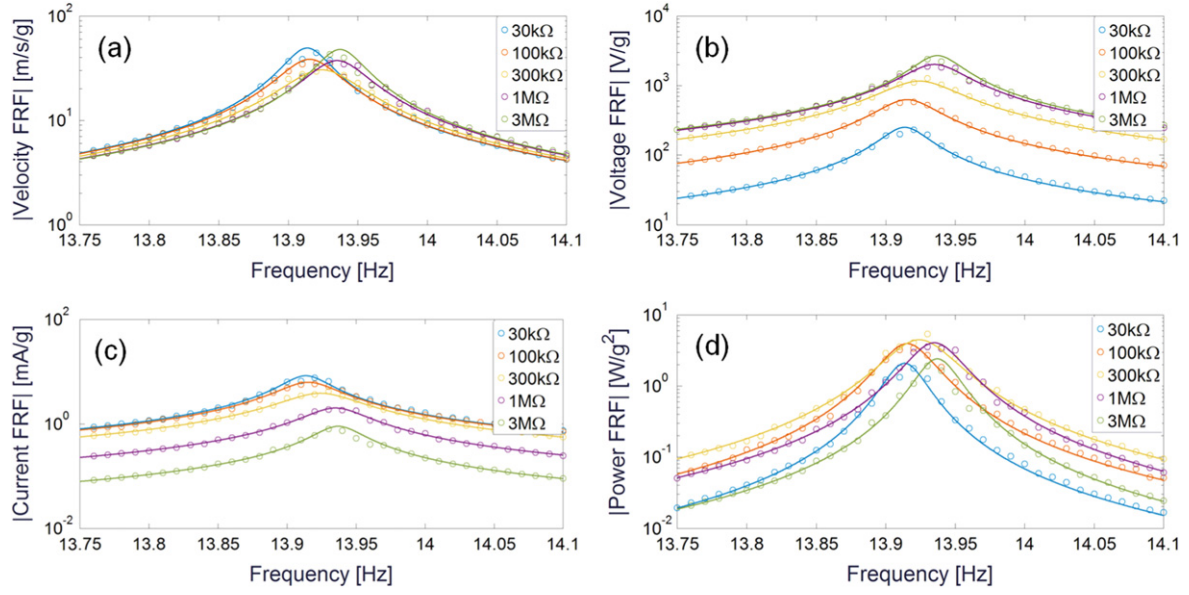
Figure 5. Linear electromechanical FRFs: (a) velocity, (b) voltage, (c) current, and (d) power output per base acceleration at various load resistance levels (obtained by very low intensity white noise excitation). Circles represent experimental data and solid curves represent model predictions.
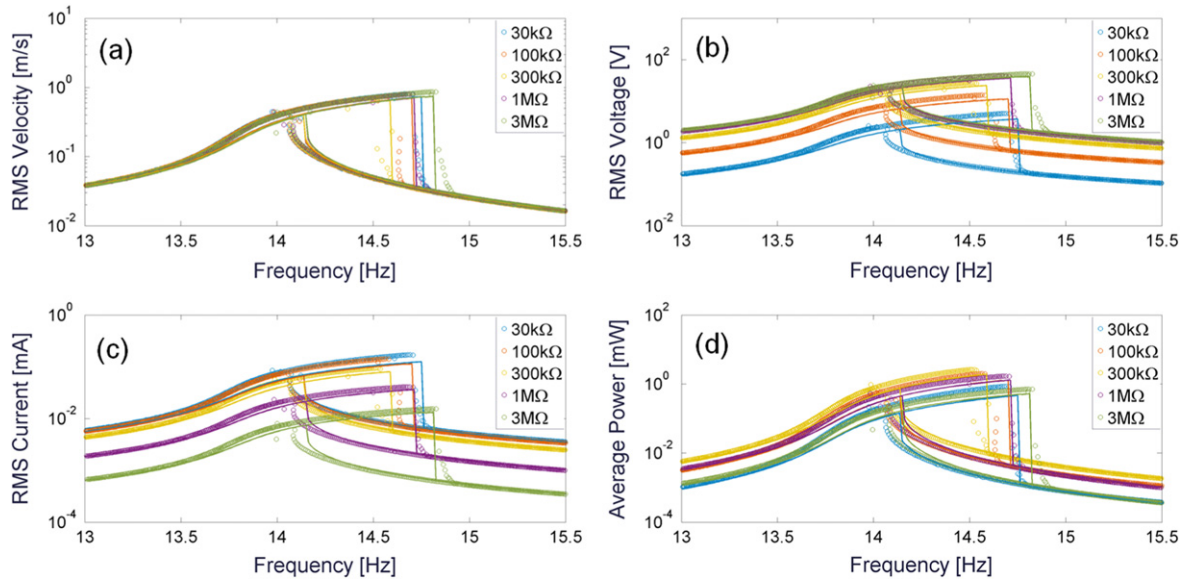

Figure 6. Nonlinear electromechanical frequency response curves in the neighborhood of primary resonance excitation ($\Omega \approx \omega_n$): (a) velocity, (b) voltage, (c) current, and (d) power output (base acceleration: 0.04g RMS). Circles represent experimental data and solid curves represent model predictions.

3.5.1. Primary resonance. By using the feedback shaker system (figure 3), up and down frequency sweep experiments are conducted at RMS (root-mean-square) base acceleration levels of 0.01g, 0.02g, 0.03g, and 0.04g. Only the results of the 0.04g experiments are shown in figure 6 for brevity. There is a very good match between the model predicted behavior (5-term harmonic balance solution) and the experimental results at all studied base acceleration levels and load resistance values. The main discrepancy is that the model underestimates the response magnitude somewhat in every case. While both the nonlinear restoring force and dissipative forces play a role in this, even with no velocity squared

dissipation ($h_a = 0$), the model still under predicts the response. Part of the error can be attributed to unmodeled inertial nonlinearity. Because the potential (and expectedly minor) ferroelastic (stress–strain) nonlinearity due to piezoelectric laminates would be captured within the force–displacement relationship, part of the unmodeled nonlinearity might be due to electromechanical coupling [43] associated with increased forcing. The energy harvesting performance of the M-shaped device at near optimal load conditions and various base acceleration amplitudes is summarized in table 3. Due to the dominant hardening nonlinearity and jump phenomenon, a saturation of the response amplitude and a

Table 3. Summary of experimental results and model predictions at various base acceleration levels (load resistance: 300 kΩ).

g_{RMS}		0.01	0.02	0.03	0.04
$\dot{x}_{RMS}$ (mm s^{-1})	Experiment	244	415	564	708
	Model	230	395	536	647
v_{RMS} (V)	Experiment	9.2	15.9	22.0	28.0
	Model	8.7	14.9	20.0	23.0
i_{RMS} (μA)	Experiment	30.5	52.8	73.4	93.3
	Model	29.0	49.6	66.6	79.8
P_{AVG} (mW)	Experiment	0.28	0.84	1.62	2.61
	Model	0.25	0.74	1.33	1.91
f_{PEAK} (Hz)	Experiment	14.00	14.13	14.31	14.51
	Model	14.01	14.20	14.40	14.59
Δf (Hz)	Experiment	0.12	0.18	0.27	0.38
	Model	0.08	0.19	0.28	0.37

widening of the response bandwidth are observed. Despite the aforementioned errors, the model shows the correct trends and provides very good predictions of harvester performance. For the largest excitation level studied in this work (0.04g RMS case, i.e. figure 6), the bandwidth of the system for 300 kΩ load resistance is 0.38 Hz, which is 660 % larger than the linear bandwidth (0.05 Hz) summarized in the previous section.

Note that the nonlinear frequency response bandwidth is shorter for the optimal load case inevitably due to dissipation as a result of Joule heating in the resistor that is used to quantify the electrical power output. This phenomenon is inevitable in more complex nonlinear energy harvesting circuits [61, 62] as well (due to power transfer from the mechanical to electrical domain) and is the nonlinear counterpart of damping resulting from energy harvesting (see Lesieutre *et al* [63] for its linear counterpart in the sense of classical shunt damping). As one moves away from the optimal electrical load condition, the nonlinear bandwidth increases at the expense of reduced power output as a tradeoff.

The individual harmonics contributing the relative displacement and voltage output frequency response curves in the 5-term ($N=5$) harmonic balance solution are reported in figure 7. Note that the voltage response has no DC (zero frequency) component whereas the DC component in the displacement response is the second major content in the frequency response after the first harmonic. Crossing of the curves at certain frequencies is also noteworthy. The effects of individual harmonics on the dynamics of the M-shaped oscillator is discussed in detail elsewhere [54]. Next we consider the secondary resonance behavior, specifically superharmonic response in the M-shaped piezoelectric energy harvester.

3.5.2. Secondary resonance for superharmonic response. Superharmonic and subharmonic resonance behaviors [22] can be observed in the M-shaped piezoelectric energy harvester. However, we consider only the superharmonic resonance range as it may have more practical implications

(such as MEMS configurations or other compact designs under high excitation intensities with frequency content well below the primary resonance frequency neighborhood). In order to study the 1:2 and 1:3 superharmonic resonance behaviors of the M-shaped energy harvester, simulations and frequency sweep tests are conducted for frequency ranges near one half of the linear natural frequency and one third of the linear natural frequency. To become apparent, secondary resonances typically require higher forcing amplitudes, as they are effectively excited internally by the nonlinearities acting on the quasilinear response, as opposed to being excited by the external forcing directly as with the primary resonance. Tests and simulations are therefore carried out at RMS base acceleration levels of 0.1, 0.2, 0.3, and 0.4g. Figure 8 shows the displacement and voltage response frequency contents predicted by the 5-term harmonic balance analysis for the cubic and quadratic superharmonic resonance neighborhoods for 0.4g RMS base acceleration.

As anticipated previously in section 3.3 based on the quadratic and cubic stiffness terms in table 1, the quadratic nonlinearity is more significant than the cubic nonlinearity for response levels on the order ~0.1 cm (which is indeed the displacement response level under 0.4g RMS excitation in the range of 4–8 Hz). Therefore, figure 8 confirms the fact that the predominant secondary resonance behavior should be expected in the neighborhood of $\Omega \approx \omega_n/2 \cong 7$Hz; that is, quadratic superharmonic resonance is expected to be the dominant secondary resonance. Figure 9 shows the experimental RMS velocity, voltage, current, and average power output frequency response curves of the M-shaped harvester along with model predictions. Surprisingly, the experimental data shows significant mismatch around $\Omega \approx \omega_n/3 \cong 4.7$Hz with an unexpected resonance behavior contradicting the previous argument, which is explained next.

In figure 9, unlike model predictions, the experimental data shows large responses for both the quadratic and cubic superharmonic resonances, with the cubic resonance unexpectedly being the larger of the two. As discussed previously in section 2.5, superharmonic resonance experiments are made more complicated as harmonic distortion in the excitation signal generates response at the same frequencies as those created by the nonlinearities of interest in the harvester. Therefore the major suspect that might cause this unexpected resonance around $\Omega \approx \omega_n/3 \cong 4.7$Hz is potentially the distortion in the excitation signal itself (i.e. failure of the shaker to produce pure harmonic excitation at low frequencies). The time histories of base acceleration signals at 4.7 Hz (i.e. $\Omega \approx \omega_n/3$) and 7 Hz (i.e. $\Omega \approx \omega_n/2$) are shown in figure 10 along with their FFTs. For frequencies under approximately 5 Hz, the shaker and vibration controller used for these experiments are unable to produce a suitably pure sinusoidal acceleration. The motion of the shaker is corrupted by a number of sources of error, including measurement noise from the accelerometer (sent to the controller), quantization errors in the digital controller, and perhaps most important for the low frequencies as in these experiments, dry friction in the shaker armature. Dry friction in the shaker armature can cause unwanted stop-start (or
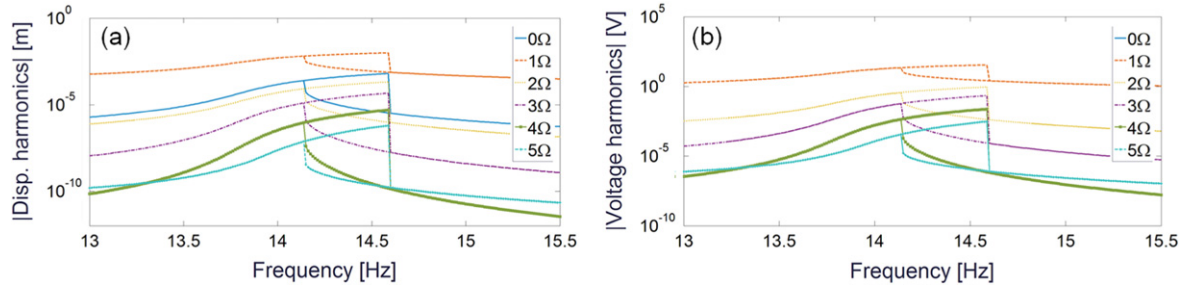
Figure 7. Harmonic content of (a) relative displacement and (b) voltage output obtained by model simulation for the neighborhood of primary resonance excitation ($\Omega \approx \omega_n$, base acceleration: 0.04g RMS, load resistance: 300 kΩ).
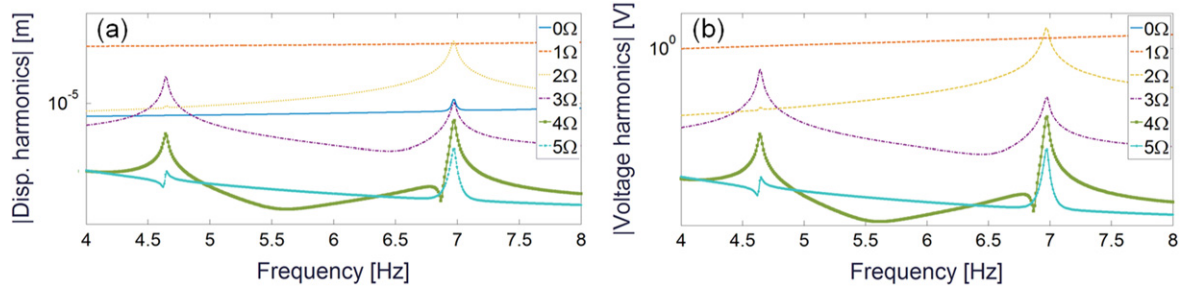

Figure 8. Frequency content of (a) relative displacement and (b) voltage output obtained by model simulation for the neighborhood of secondary resonance excitation (covering $\Omega \approx \omega_n/3$ and $\Omega \approx \omega_n/2$, base acceleration: 0.4$g$ RMS, load resistance: 300 kΩ).
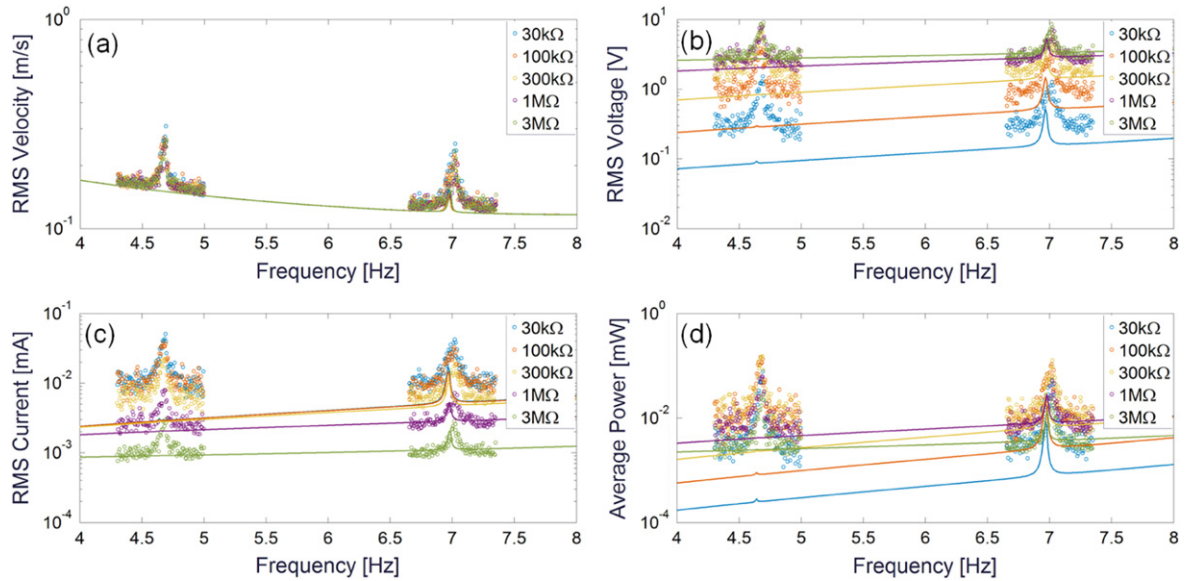

Figure 9. Nonlinear electromechanical frequency response curves in the neighborhood of secondary resonance excitation: (a) velocity, (b) voltage, (c) current, and (d) power output (base acceleration: 0.4g RMS). Substantial mismatch for $\Omega \approx \omega_n/3$ is due to the shaker's limitation in low-frequency (roughly for <5 Hz) excitation that results in higher harmonics in base acceleration. Circles represent experimental data and solid curves represent model predictions.

'stick-slip') like motion. This causes the desired sinusoidal output acceleration to become distorted into a shape more resembling a square wave, i.e. a signal with content at three times the fundamental frequency (figure 10(a)). It is therefore concluded that the peak at $\omega_n/3$ seen in experiments is not due to secondary resonance nonlinear behavior, but rather due to harmonic distortion in the input base acceleration exciting the primary resonance directly. Next,

knowing the frequency content (figure 10) of the multi-harmonic excitation caused by the shaker, the frequency response in 4–8 Hz (figure 9) can be modeled more accurately as a combined exercise of multi-harmonic excitation and superharmonic secondary resonance.

In order to better model the experimental behavior around 4.7 Hz (i.e. $\Omega \approx \omega_n/3$) and 7 Hz (i.e. $\Omega \approx \omega_n/2$), the true (non-ideal) representation of the base acceleration can be
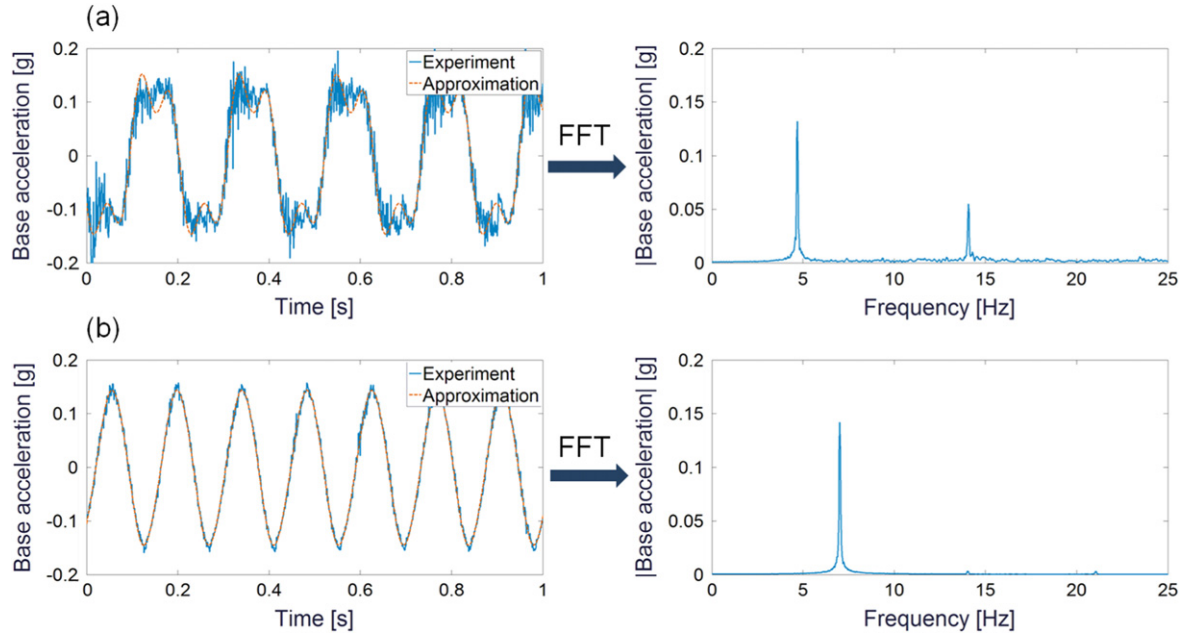
Figure 10. Base acceleration time series produced by the shaker for excitation at (a) 4.7 Hz (i.e. $\Omega \approx \omega_h/3$) and (b) 7 Hz (i.e. $\Omega \approx \omega_h/2$) along with their FFTs (0.1g RMS base acceleration). Clearly the time series at 4.7 Hz results in multi-harmonic excitation of the harvester due to the shaker's inability to produce pure harmonic excitation at low frequencies.

Table 4. Coefficients of higher harmonics in base acceleration to explore the superharmonic resonance accounting for the multi-harmonic nature of true (experimental) excitation.

	$3\Omega = \omega_n$		$2\Omega = \omega_n$	
g_{RMS}	α_2	α_3	α_2	α_3
0.1	0.0342	0.3823	0.0214	0.0206
0.2	0.0296	0.1095	0.0116	0.0572
0.3	0.0178	0.0320	0.0248	0.0240
0.4	0.0069	0.0456	0.0340	0.0257

used based on figure 10:

$$\ddot{y}(t) = A\Big[\cos(\Omega t) + \alpha_2 \cos\big(2\Omega t + \phi_2\big)$$
$$+ \alpha_3 \cos\big(3\Omega t + \phi_3\big)\Big]. \quad (29)$$

Here, A is the nominal acceleration amplitude (at the intended single-frequency excitation), and α_2 and α_3 are the amplitudes of the harmonics of interest expressed as fractions of the nominal acceleration (for ideal single frequency excitation, $\alpha_2 = \alpha_3 = 0$). The values of the coefficients of the higher harmonic components in the base acceleration signal are found by recording time histories of steady-state base acceleration signals at the frequencies of interest and extracting their frequency content (as shown in figure 10 for 0.1g RMS base acceleration). The coefficients needed to properly model the base acceleration seen in the performed experiments are summarized in table 4.

Using this more accurate model of the base acceleration signal and the ability of the method of harmonic balance to simulate the response of the M-shaped harvester to multi-harmonic excitation, the observed behavior can be simulated.

The experimental RMS velocity, voltage, current, and average power output and model predictions with the multi-harmonic base acceleration model are shown in figure 11. The 3-harmonic model for the base acceleration signal (given by equation (29)) used in the 5-term harmonic balance solution results in a much better prediction of the observed experimental responses amplitudes. The model simulation still differs from the observed response in that the model predicts hardening jump phenomenon behavior, while the experimental data shows no clear jump, which may be attributed to the fact that the experimental base acceleration is significantly noisier than the ideal 3-harmonic excitation used in the model.

An interesting observation is regarding the optimal resistance of the maximum power output. When attempting to harvest energy from superharmonic resonances, the optimal load impedance for the energy harvester will be close to the optimal load impedance for the same harvester under primary resonance excitation. This is because the optimal load impedance depends on the dominant frequency content of the harvester's response, not the dominant frequency content of the excitation. For a properly tuned linear resonant vibration energy harvester (and for a nonlinear harvester operating under primary resonance excitation), the dominant frequency of the response will match the dominant frequency of excitation, but this is not the case for secondary resonance behavior of a nonlinear energy harvester as it is the response frequency content that matters. Beyond the intriguing nature of secondary resonance excitations as a nonlinear dynamics exercise, superharmonic resonance behavior may be exploited for energy harvesting purposes as it allows low frequency ambient vibrations to excite energy harvesting devices that might have higher natural frequencies due to size and mass
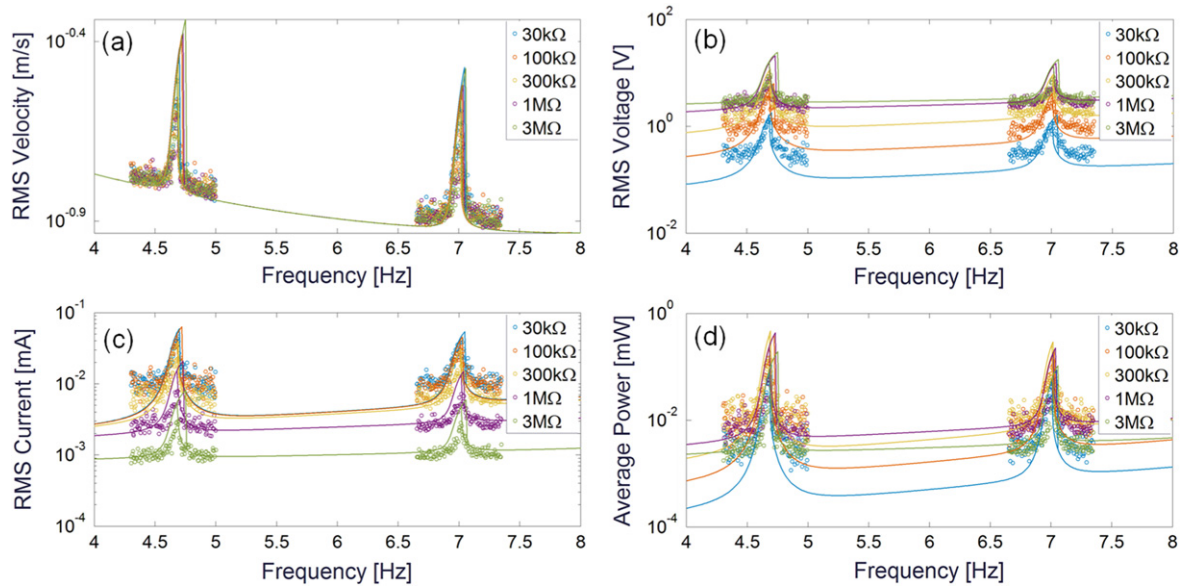
Figure 11. Nonlinear electromechanical frequency response curves in the neighborhood of secondary resonance excitation (covering $\Omega \approx \omega_n/3$ and $\Omega \approx \omega_n/2$) by accounting for multi-harmonic excitation effects of the shaker in modeling: (a) velocity, (b) voltage, (c) current, and (d) power output (base acceleration: $0.4g$ RMS). Circles represent experimental data and solid curves represent model predictions.

constraints (e.g. MEMS energy harvesters) in the sense of nonlinear frequency-up converter [41]. Since secondary resonances require higher forcing amplitudes to become apparent, power generation efficiency will be smaller than for primary resonance excitation.

4. Conclusions

Nonlinear frequency bandwidth enhancement in vibration energy harvesting can be achieved most effectively in the presence of strong nonlinearities and under high excitation levels. This constitutes a fundamental challenge in enabling nonlinear energy harvesters for low-intensity environments. To overcome the need for high excitation intensities that are required to exploit nonlinear dynamic phenomena, we developed an M-shaped piezoelectric energy harvester configuration that can exhibit a nonlinear frequency response under very low vibration levels (below $0.1g$). This configuration was made from a continuous bent spring steel with piezoelectric laminates and a proof mass but no magnetic components. Properly locating the piezoelectric patches (to avoid substantial piezoelectric softening) in this design enables achieving the jump phenomenon in hardening at a few milli-g base acceleration levels.

We explored for both primary and secondary (super-harmonic) resonance excitations at different vibration levels and load resistance values. The primary resonance excitation case that offers a 660 % increase in the half-power bandwidth as compared to the linear system at a root-mean-square excitation level as low as $0.04g$. The secondary resonance behavior was investigated with a focus on 1:2 and 1:3 superharmonic resonances. Following the development of an empirical model, a multi-term harmonic balance framework

was developed for a computationally effective yet high-fidelity analysis of this high-quality-factor system with cubic and quadratic nonlinearities. Experimental measurements and electromechanical model predictions resulted in very good match for both primary and secondary resonance cases explored in this work.

Overall, substantial nonlinear bandwidth is achieved for very low base acceleration levels under primary resonance excitation. The secondary resonance of interest in this work was superharmonic resonance for nonlinear frequency-up conversion. It has been pointed out that the optimal electrical load of superharmonic response is close to that of the same harvester under primary resonance excitation. This is because the optimal load impedance depends on the dominant frequency content of the harvester's response, rather than the dominant frequency content of the excitation (no such distinction exists in linear harvesters or nonlinear ones under primary resonance excitation). Superharmonic resonance behavior may be exploited for energy harvesting purposes as it allows low frequency ambient vibrations to excite energy harvesting devices that might have higher natural frequencies due to size and mass constraints (e.g. MEMS energy harvesters), as a nonlinear frequency-up conversion mechanism.

In low-frequency superharmonic resonance experiments, an experimental imperfection of the electrodynamic shaker (which fails to produce pure harmonic signal for excitations roughly below 5 Hz) was pointed out and used as an opportunity to formulate and explore nonlinear response to multi-harmonic excitation in the secondary resonance regime. Multi-term harmonic balance solution resulted in very good match for the complex case of multi-harmonic excitation combined with secondary resonance behavior.

Acknowledgments

References

[1] Roundy S, Wright P K and Rabaey J M 2003 *Energy Scavenging for Wireless Sensor Networks* (Berlin: Springer)

[2] Erturk A and Inman D J 2011 *Piezoelectric Energy Harvesting* (New York: Wiley)

[3] Elvin N and Erturk A 2013 *Advances in Energy Harvesting Methods* (New York: Springer)

[4] Glynne-Jones P *et al* 2004 An electromagnetic, vibration-powered generator for intelligent sensor systems *Sensors Actuators* A **110** 344–9

[5] Arnold D P 2007 Review of microscale magnetic power generation *IEEE Trans. Magn.* **43** 3940–51

[6] Moss S D *et al* 2015 Scaling and power density metrics of electromagnetic vibration energy harvesting devices *Smart Mater. Struct.* **24** 023001

[7] Roundy S, Wright P K and Rabaey J 2003 A study of low level vibrations as a power source for wireless sensor nodes *Comput. Commun.* **26** 1131–44

[8] Mitcheson P D *et al* 2004 MEMS electrostatic micropower generator for low frequency operation *Sensors Actuators* A **115** 523–9

[9] Le C P *et al* 2012 Microscale electrostatic energy harvester using internal impacts *J. Intell. Mater. Syst. Struct.* **23** 1409–21

[10] Roundy S and Wright P K 2004 A piezoelectric vibration based generator for wireless electronics *Smart Mater. Struct.* **13** 1131–42

[11] DuToit N E and Wardle B L 2007 Experimental verification of models for microfabricated piezoelectric vibration energy harvesters *AIAA J.* **45** 1126–37

[12] Erturk A and Inman D J 2009 An experimentally validated bimorph cantilever model for piezoelectric energy harvesting from base excitations *Smart Mater. Struct.* **18** 025009

[13] Adhikari S, Friswell M and Inman D 2009 Piezoelectric energy harvesting from broadband random vibrations *Smart Mater. Struct.* **18** 115005

[14] Wang L and Yuan F G 2008 Vibration energy harvesting by magnetostrictive material *Smart Mater. Struct.* **17** 045009

[15] Adly A *et al* 2010 Experimental tests of a magnetostrictive energy harvesting device toward its modeling *J. Appl. Phys.* **107** 09A935

[16] Kornbluh R D *et al* 2011 From boots to buoys: promises and challenges of dielectric elastomer energy harvesting *Proc. SPIE 7976: Electroactive Polymer Actnators and Devices (EAPAD) 2011* (doi:10.1117/12.882367)

[17] Aureli M *et al* 2010 Energy harvesting from base excitation of ionic polymer metal composites in fluid environments *Smart Mater. Struct.* **19** 015003

[18] Anton S, Farinholt K and Erturk A 2014 Piezoelectret foam–based vibration energy harvesting *J. Intell. Mater. Syst. Struct.* **25** 1681–92

[19] Deng Q *et al* 2014 Nanoscale flexoelectric energy harvesting *Int. J. Solids Struct.* **51** 3218–25

[20] Anton S R and Sodano H A 2007 A review of power harvesting using piezoelectric materials (2003–2006) *Smart Mater. Struct.* **16** R1

[21] Cook-Chennault K, Thambi N and Sastry A 2008 Powering MEMS portable devices—a review of non-regenerative and regenerative power supply systems with special emphasis on piezoelectric energy harvesting systems *Smart Mater. Struct.* **17** 043001

[22] Nayfeh A H and Mook D T 2008 *Nonlinear Oscillations* (New York: Wiley)

[23] Guckenheimer J and Holmes P 1983 *Nonlinear Oscillations, Dynamical Systems, and Bifurcations of Vector Fields* vol 42 (New York: Springer)

[24] Nayfeh A H and Balachandran B 2008 *Applied Nonlinear Dynamics: Analytical, Computational and Experimental Methods* (New York: Wiley)

[25] Daqaq M F *et al* 2014 On the role of nonlinearities in vibratory energy harvesting: a critical review and discussion *Appl. Mech. Rev.* **66** 040801

[26] Burrow S *et al* 2008 Vibration energy harvesters with non-linear compliance *Proc. SPIE 6928: Active and Passive Smart Structures and Integrated Systems 2008* (doi:10.1117/12.776881)

[27] Mann B and Sims N 2009 Energy harvesting from the nonlinear oscillations of magnetic levitation *J. Sound Vib.* **319** 515–30

[28] Cottone F, Vocca H and Gammaitoni L 2009 Nonlinear energy harvesting *Phys. Rev. Lett.* **102** 080601

[29] Erturk A, Hoffmann J and Inman D 2009 A piezomagnetoelastic structure for broadband vibration energy harvesting *Appl. Phys. Lett.* **94** 254102

[30] Stanton S C, McGehee C C and Mann B P 2009 Reversible hysteresis for broadband magnetopiezoelastic energy harvesting *Appl. Phys. Lett.* **95** 174103-174103-3

[31] Erturk A, Hoffmann J and Inman D J 2009 A piezomagnetoelastic structure for broadband vibration energy harvesting *Appl. Phys. Lett.* **94** 254102

[32] Stanton S C, McGehee C C and Mann B P 2010 Nonlinear dynamics for broadband energy harvesting: investigation of a bistable piezoelectric inertial generator *Physica D: Nonlinear Phenom.* **239** 640–53

[33] Erturk A and Inman D J 2011 Broadband piezoelectric power generation on high-energy orbits of the bistable Duffing oscillator with electromechanical coupling *J. Sound Vib.* **330** 2339–53

[34] Stanton S C, Owens B A and Mann B P 2012 Harmonic balance analysis of the bistable piezoelectric inertial generator *J. Sound Vib.* **331** 3617–27

[35] Sneller A, Cette P and Mann B 2011 Experimental investigation of a post-buckled piezoelectric beam with an attached central mass used to harvest energy *Proc. Inst. Mech. Eng. I: J. Syst. Control Eng.* **225** 497–509

[36] Arrieta A *et al* 2010 A piezoelectric bistable plate for nonlinear broadband energy harvesting *Appl. Phys. Lett.* **97** 104102

[37] Mann B and Owens B 2010 Investigations of a nonlinear energy harvester with a bistable potential well *J. Sound Vib.* **329** 1215–26

[38] Nguyen S D, Halvorsen E and Paprotny I 2013 Bistable springs for wideband microelectromechanical energy harvesters *Appl. Phys. Lett.* **102** 023904-023904-4

[39] Cottone F, Vocca H and Gammaitoni L 2009 Nonlinear energy harvesting *Phys. Rev. Lett.* **102** 080601

[40] Ramlan R *et al* 2010 Potential benefits of a non-linear stiffness in an energy harvesting device *Nonlinear Dyn.* **59** 545–58

[41] Barton D A, Burrow S G and Clare L R 2010 Energy harvesting from vibrations with a nonlinear oscillator *J. Vib. Acoust.* **132** 021009

[42] Masana R and Daqaq M 2012 Energy harvesting in the super-harmonic frequency region of a twin-well oscillator *J. Appl. Phys.* **111** 044501

[43] Stanton S C *et al* 2010 Nonlinear piezoelectricity in electroelastic energy harvesters: modeling and experimental identification *J. Appl. Phys.* **108** 074903

[44] Stanton S C *et al* 2010 Resonant manifestation of intrinsic nonlinearity within electroelastic micropower generators *Appl. Phys. Lett.* **97** 254101

[45] Stanton S C *et al* 2012 Nonlinear nonconservative behavior and modeling of piezoelectric energy harvesters including proof mass effects *J. Intell. Mater. Syst. Struct.* **23** 183–99

[46] Leadenham S and Erturk A 2015 Unified nonlinear electroelastic dynamics of a bimorph piezoelectric cantilever for energy harvesting, sensing, and actuation *Nonlinear Dyn.* **79** 1727–43

[47] McInnes C, Gorman D and Cartmell M P 2008 Enhanced vibrational energy harvesting using nonlinear stochastic resonance *J. Sound Vib.* **318** 655–62

[48] Litak G, Friswell M and Adhikari S 2010 Magnetopiezoelastic energy harvesting driven by random excitations *Appl. Phys. Lett.* **96** 214103

[49] Cottone F *et al* 2012 Piezoelectric buckled beams for random vibration energy harvesting *Smart Mater. Struct.* **21** 035021

[50] Daqaq M F 2012 On intentional introduction of stiffness nonlinearities for energy harvesting under white Gaussian excitations *Nonlinear Dyn.* **69** 1063–79

[51] Zhao S and Erturk A 2013 On the stochastic excitation of monostable and bistable electroelastic power generators: relative advantages and tradeoffs in a physical system *Appl. Phys. Lett.* **102** 103902

[52] Halvorsen E 2013 Fundamental issues in nonlinear wideband-vibration energy harvesting *Phys. Rev.* E **87** 042129

[53] Nguyen D *et al* 2010 Fabrication and characterization of a wideband MEMS energy harvester utilizing nonlinear springs *J. Micromech. Microeng.* **20** 125009

[54] Leadenham S and Erturk A 2014 M-shaped asymmetric nonlinear oscillator for broadband vibration energy harvesting: harmonic balance analysis and experimental validation *J. Sound Vib.* **333** 6209–23

[55] Kundert K S and Sangiovanni-Vincentelli A 1986 Simulation of nonlinear circuits in the frequency domain *IEEE Trans. Comput.-Aided Des. Integr. Circuits Syst.* **5** 521–35

[56] Tang D, Zhao M and Dowell E H 2014 Inextensible beam and plate theory: computational analysis and comparison with experiment *J. Appl. Mech.* **81** 061009

[57] Guyomar D *et al* 2005 Toward energy harvesting using active materials and conversion improvement by nonlinear processing *IEEE Trans. Ultrason. Ferroelectr. Freq. Control* **52** 584–95

[58] Nayfeh A H 2008 *Perturbation Methods* (New York: Wiley)

[59] Morison J, Johnson J and Schaaf S 1950 The force exerted by surface waves on piles *J. Pet. Technol.* **2** 149–54

[60] Bandstra J 1983 Comparison of equivalent viscous damping and nonlinear damping in discrete and continuous vibrating systems *J. Vib. Acoust.* **105** 382–92

[61] Ottman G K *et al* 2002 Adaptive piezoelectric energy harvesting circuit for wireless remote power supply *IEEE Trans. Power Electron.* **17** 669–76

[62] Kong N *et al* 2010 Resistive impedance matching circuit for piezoelectric energy harvesting *J. Intell. Mater. Syst. Struct.* **21** 1293–1302

[63] Lesieutre G A, Ottman G K and Hofmann H F 2004 Damping as a result of piezoelectric energy harvesting *J. Sound Vib.* **269** 991–1001